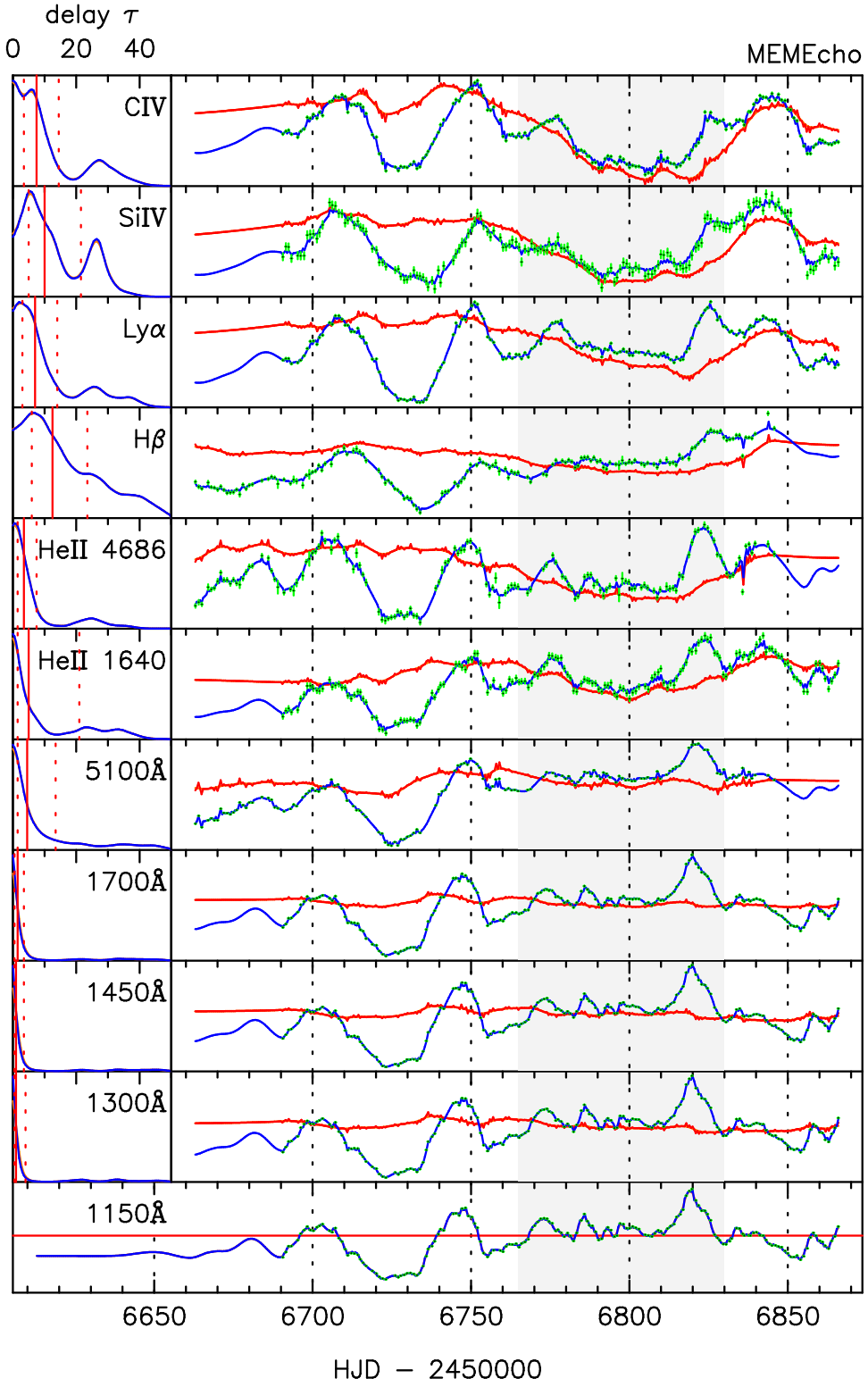

Figure 4. MEMECHO fits to five continuum and six emission-line light curves of NGC 5548. The driving light curve (bottom panel) is the 1150 Å continuum light curve with a reference level (red line) at the median of the 1150 Å continuum data. Above this are 10 echo light curves (right) and corresponding delay maps (left), comparing the light-curve data (the black points with green error bars) and the echo model (blue curves) with slow background variations (red curves). The echoes (bottom up) are four continuum light curves, at 1300, 1450, and 1700 Å from the HST spectra and at 5100 Å from the MDM spectra, then six reverberating emission lines (He II $\lambda\lambda$1640, 4686, Hβ, Lyα, Si IV, and C IV). On each delay map in the left column, the median delay is marked by a vertical line, flanked by vertical dashed lines for the quartiles of the delay distribution. The MEMECHO fit accounts for much of the light-curve structure as echoes of the driving light curve but requires significant additional variations (red curves). The gray shaded region indicates the time span of the "BLR Holiday" identified in Paper IV.

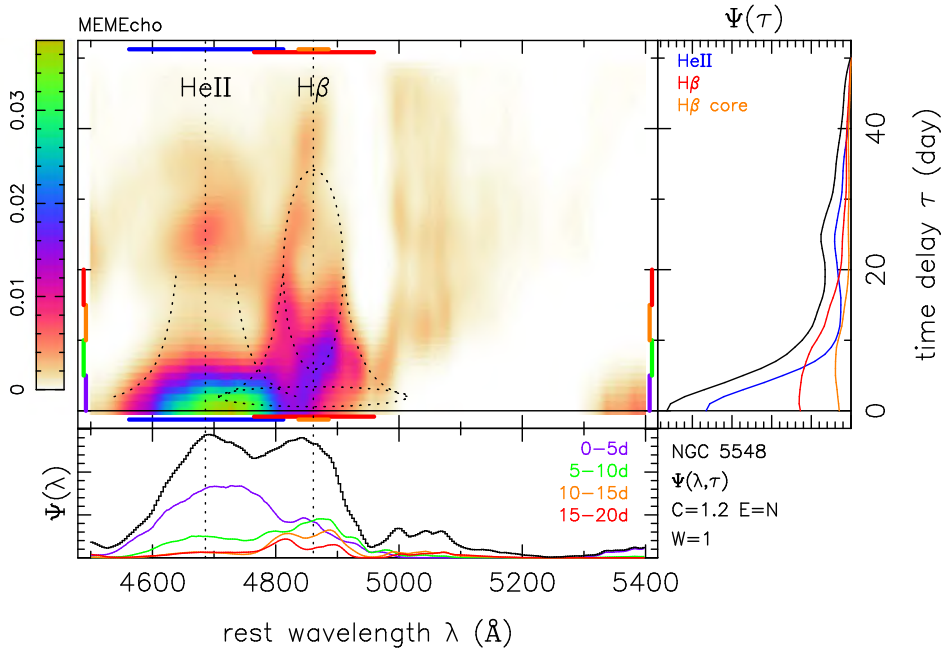

Figure 5. Two-dimensional wavelength–delay map $\Psi(\lambda, \tau)$ reconstructed from the MEMECHO fit to the optical spectra from MDM. Delays are measured relative to the 1150 Å continuum light curve. Panels below and to the right of the map give the projected responses $\Psi(\lambda)$ and $\Psi(\tau)$. Here the black curve is the full response, and the colored curves are for the wavelength or delay ranges indicated by the correspondingly colored bars in the margins of the map. Dotted curves show the envelope around each line inside which emission can occur from a Keplerian disk inclined by $i = 45°$ orbiting a black hole of mass $M_{\rm BH} = 7 \times 10^7\, M_\odot$. The ellipses shown for Hβ correspond to Keplerian disk orbits at $R = 2$ and 20 lt-day. The units of $\Psi(\lambda, \tau)$, indicated on the color bar, are 1/day.

4. Velocity–Delay Maps

Velocity–delay maps project the information that is coded in the reverberating emission-line profile onto a two-dimensional map of the six-dimensional position–velocity phase space of the BLR gas. While this is incomplete information, an ordered velocity field can have an easily recognizable signature in the velocity–delay map; some examples are shown by Welsh & Horne (1991). A signature of inflowing gas is short delays on the red wing of the velocity profile and a wide range of delays on the blue side. Outflowing gas has a similar but reversed signature. An orbiting ring of gas at radius R maps into an ellipse on the velocity–delay plane, centered at $\tau = R/c$ and extending over $(R/c)(1 \pm \sin i)$, allowing the identification of R and i. A Keplerian disk superimposes these ellipses to form a "virial envelope" that can be used to infer $V \sin i$ at each R. Assuming $V = \sqrt{G\, M_{\rm BH}/R}$, this gives $M_{\rm BH}/\sin^2 i$. Thus, a sufficiently crisp velocity–delay map can be read to infer the general nature of the flow in the BLR, and several specific parameters of the geometry and kinematics. With velocity–delay maps for several lines, the radial ionization structure in the BLR becomes manifest, and subtle structures such as spiral density waves may become evident (Horne et al. 2004). Constructing velocity–delay maps was therefore the principal motivation for undertaking the STORM campaign.

4.1. MEMECHO Fits to the Spectral Variations

Wavelength–delay maps $\Psi(\lambda, \tau)$ of the emission-line response in NGC 5548 are shown as two-dimensional false-color images in Figure 5 for the MEMECHO fit to the optical spectra from MDM and in Figure 6 for the UV spectra from HST.

In the panel to the right of the 2D map, the projections $\Psi(\tau)$ give delay maps for the full wavelength range (black) and for velocity ranges centered on the rest wavelengths of the emission lines, as indicated by the colored bars above and below the map. In the panel below, the projections $\Psi(\lambda)$ give the spectrum of the full response (black) and of the response in four delay ranges, 0–5 days (purple), 5–10 days (green), 10–15 days (orange), and 15–20 days (red). Velocity–delay maps centered on the six emission lines are presented in Figure 7. These two-dimensional maps show that the emission-line response inhabits the interior of a virial envelope (dashed) and exhibit structure indicating a Keplerian disk inclined by $i = 45°$ and with an outer rim at $R/c = 20$ days, as discussed below. These maps and their interpretation are the main results of interest emerging from our MEMECHO analysis.

Details from the MEMECHO fit are shown in Figures 8 and 9 for the HST and MDM spectra, respectively, with the same format as in Figure 4. The fit models as echoes the same four continuum light curves (at 1350, 1450, 1700, and 5100 Å), and now as well the continuum-subtracted emission-line variations across the full wavelength range of the HST and MDM spectra. The PREPSPEC model provided the variable continuum model that was subtracted to isolate the BLR spectra used in the MEMECHO fit. As before, the proxy driving light curve $C(t)$ is the continuum light curve at 1150 Å. The model allows echo responses over a delay range of 0–50 days and includes a time-variable background spectrum $L_0(\lambda, t)$. This allows the model to account for the period of anomalous line response during the BLR Holiday (Paper IV) and any other features in the data, real or spurious, that are not easily interpretable in terms of the linearized echo model. Figure 10 presents a grayscale "trailed spectrogram" display of the slowly varying background $L_0(\lambda, t)$ for the MEMECHO fit to the HST and MDM spectra. The Barber-Pole pattern of residuals and the BLR Holiday features are evident here.

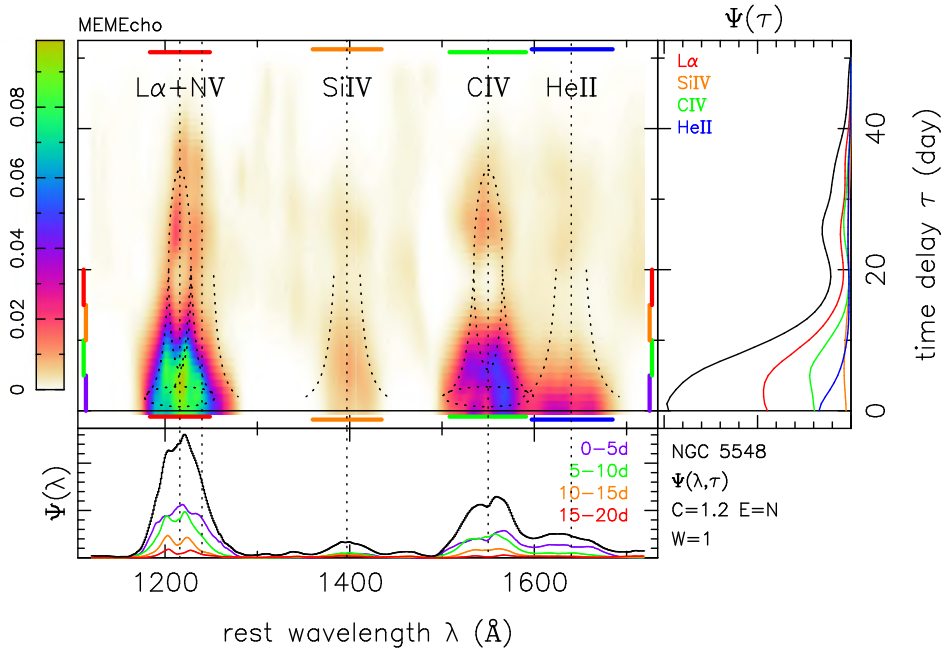

Figure 6. Same as in Figure 5, but showing the two-dimensional wavelength–delay map $\Psi(\lambda, \tau)$ reconstructed from the MEMECHO fit to the UV spectra from HST. The ellipses shown for Lyα and C IV correspond to Keplerian disk orbits at $R = 2$ and 20 lt-day.

To regularize these fits, which include two-dimensional wavelength–delay maps $\Psi(\lambda, \tau)$ and varying background spectra $L_0(\lambda, t)$, the entropy now steers the fit toward models with smooth spectra, as well as smooth light curves and delay maps. We actually construct a series of MEMECHO maps that fit the data at different values of χ^2/N, ranging from 5 to 1. At higher χ^2, the fit to the data is poor and the maps are smooth. At lower χ^2, the fit improves and the maps develop more detailed structure. When χ^2 is too low, the fit becomes strained as the model strives to fit noise features (e.g., by introducing spikes in the gaps between data points in the driving light curve). The fits and maps shown here for a fit with $\chi^2/N = 1.2$ are a good compromise between noise and resolution. Our tests show that the main features interpreted here are robust to changes in the control parameters of the fit. These parameters adjust the relative "stiffness" of the driving light curve, the background light curve, the echo maps, and the aspect ratio of resolution in the velocity and delay directions.

4.2. Interpretation of the MEMECHO Maps

From Figures 5 and 6, the three strongest lines—Lyα, C IV, and Hβ—have a similar velocity–delay structure, with most of their response occurring between 5 and 15 days. To first order, the response in all three lines is red–blue symmetric. This indicates that radial motions are subdominant in the BLR, as a strong inflow (outflow) component would produce shorter delays on the red (blue) side of the velocity profile (Welsh & Horne 1991).

The He II response is largely inside 5 days and extends to $\pm 10{,}000\,\mathrm{km\,s^{-1}}$, compatible with expected radial ionization structure and virial motions. In Figure 5, we see that He II response is broad and single peaked. He II dominates the Hβ response in the delay slice of 0–5 days (purple), becomes subdominant at 5–10 days (green), and is almost negligible at larger delays. The He II λ1640 and He II λ4686 delay ranges and velocity structures are similar. There is no signature of a double-peaked structure in these two lines.

In Figure 5, the Hβ delay maps $\Psi(\tau)$ for the full profile ($\pm 6000\,\mathrm{km\,s^{-1}}$; red) and for the line core ($\pm 1500\,\mathrm{km\,s^{-1}}$; orange) are flat or rising from 0 to 10 days and then tail away. The Hβ response spectrum $\Psi(\lambda)$ exhibits a double-peaked structure in the delay ranges of 10–15 days (orange) and 15–20 days (red), with the peaks separated by $\sim 5000\,\mathrm{km\,s^{-1}}$. In the slice of 5–10 days, the Hβ response has a central peak flanked by ledges that extend to $\pm 5000\,\mathrm{km\,s^{-1}}$. Figure 6 shows similar double-peaked responses in Lyα and somewhat less clearly in C IV.

Clearly recognizable in the velocity–delay structure is the signature of an inclined Keplerian disk with a well-defined outer edge. The velocity–delay maps provide a plausible interpretation for the "M"-shaped variation in lag with velocity seen in the cross-correlation results (Papers I and V). The outer edges of the "M" arise from the virial envelope. The "U"-shaped interior of the "M" dips down from 20 to 5 days, and we interpret this as the lower half of an ellipse in the velocity–delay plane, which is the signature of a ring of gas orbiting the black hole at radius $R = 20$ lt-day.

The Hβ response exhibits the clearest signature of an ellipse in the velocity–delay plane, corresponding to an annulus in the Keplerian disk. The (stronger) near side of the annulus has a delay at $\tau = (R/c)(1 - \sin i) \approx 5$ days, and the (weaker) far side extends to $\tau = (R/c)(1 + \sin i) \approx 35$ days. Assuming a thin disk, the ratio gives $\sin i \approx 0.75$, or $i \approx 45°$. The double-peaked velocity structure at $\tau \approx 20$ days then gives the black hole mass. The framework shown by dashed orange curves on Figures 8 and 9 was adjusted by eye to fit the main features. This provides rough estimates for the black hole mass $M_{\rm BH} \approx 7 \times 10^7\,M_\odot$, the inclination $i \approx 45°$, and the outer BLR radius $R_{\rm out} \approx 20$ lt-day. Note that the characteristic BLR response timescale, as measured by the mode or mean or median of $\Psi(\tau)$, is less than R/c at the outer edge of the BLR.

The velocity–delay structure also indicates a stronger response from the near side than from the far side of the inclined disk. We see the upper half of the ellipse only faintly

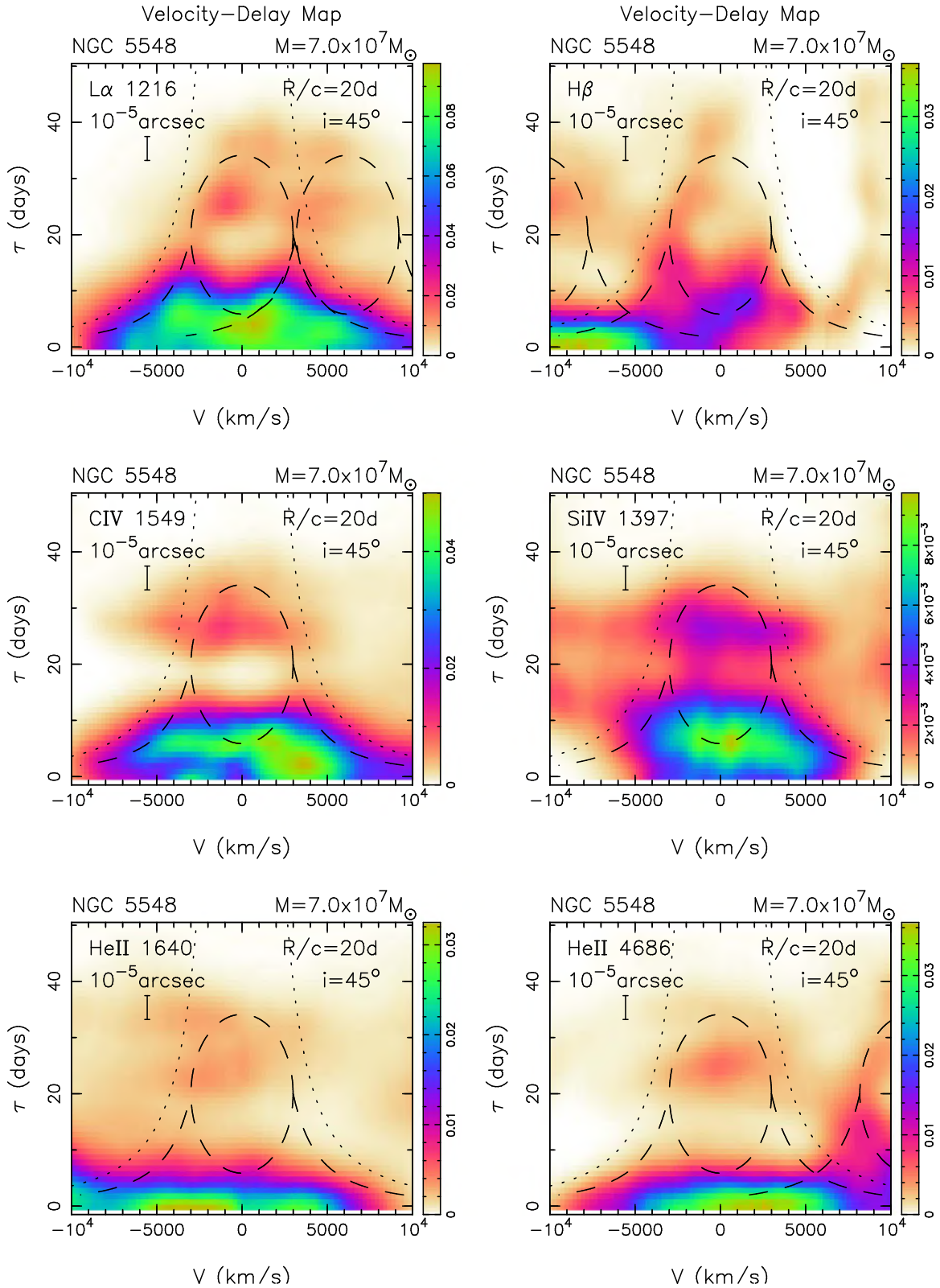

Figure 7. Velocity–delay maps $\Psi(v, \tau)$ reconstructed from the MEMECHO fit to the HST and MDM spectra. Delays are measured relative to the 1150 Å continuum light curve. Velocities are measured relative to the rest wavelength of the indicated line. Dashed black curves show the virial envelope around each line inside which emission can occur from a Keplerian disk inclined by $i = 45°$ orbiting a black hole of mass $M_{\rm BH} = 7 \times 10^7\, M_\odot$. The dashed ellipse corresponds to a circular Keplerian orbit at the outer-disk rim radius $R/c = 20$ days. Note that the red wing of Lyα is blended with N V and the blue wing of Hβ is blended with He II λ4686. A scale bar corresponding to 10 μas is shown in each panel.

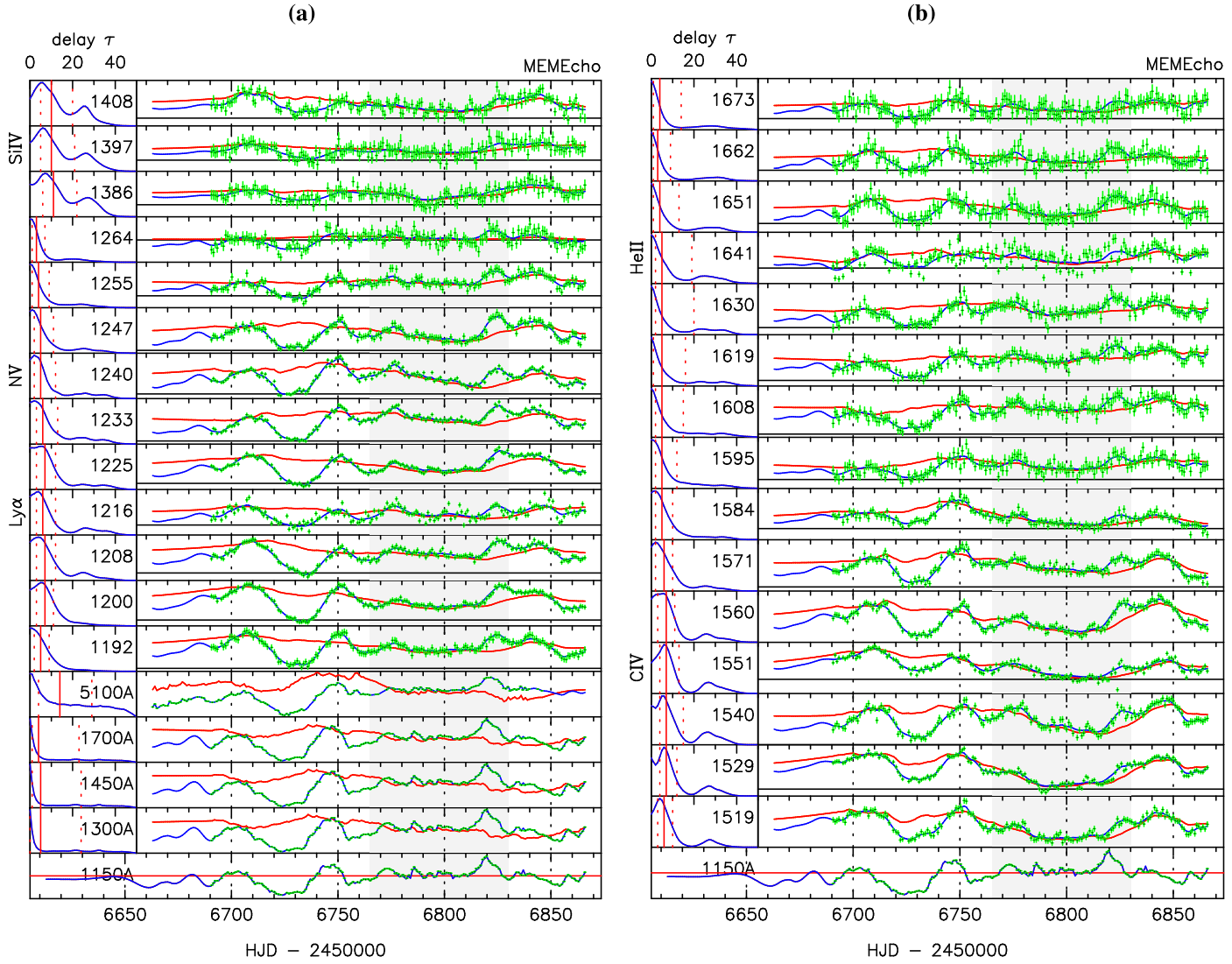

Figure 8. Details of the MEMECHO fit to the spectral variations in the HST data. Gray shading indicates the dates of the BLR Holiday. The light-curve data (black dots) with error bars (green) are compared with the fitted model (blue) and varying background (red). This global fit to $N = 125{,}448$ data points achieved a reduced $\chi^2/N = 1.2$. The bottom panel shows the driving light curve at 1150 Å. Above this are delay maps (left) and echo light curves (right). (a) Continuum echoes at 1300, 1450, 1700, and 5100 Å, and the continuum-subtracted emission at selected wavelengths, including Lyα λ1216, N V λ1240, and Si IV λ1393. (b) Echo maps and light curves for selected wavelengths, including C IV λ1549 and He II λ1640.

in the velocity–delay map of Hβ and perhaps also for Lyα. The C IV map and the (less reliable) Si IV map show a faint response at 25–30 days that is not very clearly connected to the stronger response inside 10–15 days. If the response structure were azimuthally symmetric, the upper and lower halves of the ellipse would be more equally visible. The mean delay averaged around the ellipse would be $R/c \approx 20$ days, and this is similar to typical Hβ lags seen in the past. The much shorter lags in the STORM data may be interpreted as due at least in part to an anisotropy present in 2014 that was usually much weaker or absent during previous monitoring campaigns. The near/far contrast ratio can be determined by more careful modeling.

5. Discussion

5.1. Parameter Uncertainties

The morphology of the velocity–delay maps indicates that the BLR in NGC 5548 is compatible with a disk-like geometry and kinematics, for a black hole mass $M_{\rm BH} \approx 7 \times 10^7 M_\odot$, an inclination angle $i \approx 45°$, and a relatively sharp outer rim at $R/c \approx 20$ days. Uncertainties in these parameters are difficult to quantify precisely because MEMECHO delivers the "smoothest positive" maps that fit the data at specified levels of χ^2/N. This relatively model-independent approach does not aim to determine model-specific parameters. However, by comparing the velocity–delay maps with those of toy models, we estimate that $M_{\rm BH}$ is uncertain by $\sim$20%, the inclination by $\sim 10°$, and R/c by $\sim$10%.

Future and ongoing efforts to model the STORM data will incorporate more specific geometric and kinematic parameters and photoionization physics. These should allow for parameter estimates with better-quantified uncertainties. At this stage the value of the velocity–delay maps is to inform the dynamical modeling efforts by indicating what types of models are likely to succeed.

5.2. Comparison with 2008 Mass Estimates

NGC 5548 was one of 13 AGNs monitored during the Lick AGN Monitoring Project (LAMP) 2008 RM campaign

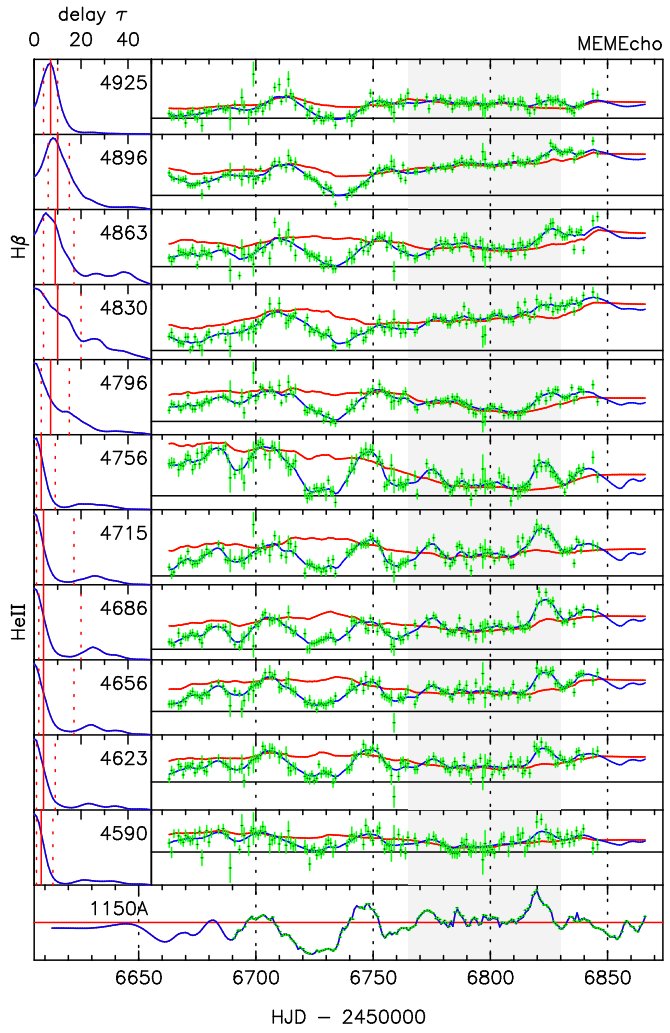

Figure 9. Details of the MEMECHO fit to the spectral variations in the MDM data. Gray shading indicates the dates of the BLR Holiday. The light-curve data (black dots) with error bars (green) are compared with the fitted model (blue) and the varying background (red). This global fit to $N = 125{,}448$ data points achieved a reduced $\chi^2/N = 1.2$. The bottom panel shows the driving light curve at 1150 Å. Above this are delay maps (left) and echo light curves (right) for continuum echoes at 1300, 1450, 1700, and 5100 Å, and for continuum-subtracted emission at selected wavelengths, including He II λ1640 and Hβ λ4861.

(Bentz et al. 2009; Walsh et al. 2009). Using spectra from the 3 m Shane telescope at Lick Observatory and Johnson V and B broadband photometry from a number of ground-based telescopes, the LAMP 2008 campaign secured 57 V-band continuum and 51 Hβ line epochs on NGC 5548 over a 70-day span. The centroid Hβ lag measured by cross-correlation methods is $\tau_{\rm cent} = 4.2^{+0.9}_{-1.3}$ days. Combined with the Hβ line width $\sigma_{\rm line} = 4270 \pm 290$ km s^{-1} from the rms spectrum, the virial product is $c\,\tau_{\rm cent}\,\sigma^2_{\rm line}/G = 14.9^{+3.7}_{-5.1} \times 10^6\ M_\odot$, giving the black hole mass as $M_{\rm BH} = 8.2^{+2.0}_{-2.8} \times 10^7 (f/5.5)\ M_\odot$, where f is the adopted calibration factor, uncertain by ∼0.3 dex for individual AGNs.

Pancoast et al. (2014) present results of a dynamical modeling fit to the 2008 LAMP data on NGC 5548. The CARAMEL code employs Markov Chain Monte Carlo methods to sample the parameters of a dynamical model of the Hβ-emitting region. Taking the V-band data as a proxy for the driving light curve, CARAMEL fits the reverberating emission-line profile variations by adjusting the spatial and kinematic distribution of Hβ-emitting clouds. This model incorporates more detailed model-specific information than the MEMECHO mapping but is flexible enough to explore a variety of inflow and outflow as well as disk-like kinematic structures. The CARAMEL fit to NGC 5548 in 2008 finds a mean delay of just 3 days, indicating a smaller Hβ emission-line region. The CARAMEL model fitted to the 2008 data has a thick-disk geometry, with an opening angle $\theta_0 = (27^{+11}_{-8})°$, a dominant H$\beta$ response on the far side of the disk, and a strong inflow signature, with small delays on the red wing relative to those on the blue wing of Hβ. The inflow and far-side response in 2008 are quite different from the symmetric disk-like kinematics and near-side response evident in the MEMECHO velocity–delay maps. Despite these differences and the smaller size of the Hβ emission-line region in 2008, the inferred mass $M_{\rm BH} = 3.9^{+2.9}_{-1.5} \times 10^7\ M_\odot$ and inclination $i = (39 \pm 12)°$ are consistent, given their uncertainties, with the corresponding values, $M_{\rm BH} \approx 7 \times 10^7\ M_\odot$ and $i \approx 45°$, that we estimate from the structure of the Hβ velocity–delay maps from the 2014 STORM data. The mass estimate from the CARAMEL fit may be too small owing to the Hβ response being measured relative to the optical continuum, which itself may have a delay of a few days. For example, in 2014 the V-band delay was 1.6 ± 0.5 days (Paper II), and that could boost the CARAMEL mass estimate by ∼50%, bringing it into closer agreement with our estimate from the velocity–delay maps.

5.3. Comparison with 2015 Velocity–Delay Maps

During 2015 January–July, a year after the STORM campaign, NGC 5548 was monitored with the Yunnan Faint Object Spectrograph and Camera on the 2.4 m telescope at Lijiang, China, resulting in 61 good spectra over 205 days that provide the basis for an MEM analysis yielding a velocity–delay map for Hβ (Xiao et al. 2018). This 2015 map exhibits structure remarkably similar to that seen in our 2014 map, including the virial envelope, the "M"-shaped structure with $\tau \approx 10$ days and $V \approx \pm 2400$ km s^{-1} at the peaks of the "M," and a well-defined ellipse extending out to $\tau \approx 40$ days.

Xiao et al. (2018) also present Hβ velocity–delay maps constructed from 13 annual AGNWatch campaigns during 1989–2001. While several of these maps show hints of a ring-like structure, the quality of these maps is much lower owing to less intensive time sampling, making it difficult to be confident about the information that they may be able to convey.

In combination, the high-fidelity 2014 and 2015 Hβ velocity–delay maps each show a clear virial envelope and distinct ellipse centered at 20 lt-day. Thus, at both epochs the Hβ response arises from a Keplerian disk with a relatively sharp outer rim at 20 lt-day that remained stable for an interval of at least a year. In 2014 the response is weak on the top of the velocity–delay ellipse. In 2015 the response is clearly visible on the blue side and over the top of the velocity–delay ellipse and relatively weak on the red side. This indicates significant azimuthal modulation of the response that evolves, perhaps rotates, on a timescale of a year. Future velocity–delay mapping experiments to monitor this structure could be interesting to elucidate its origin and implications.

5.4. Barber-Pole Patterns

The Barber-Pole pattern uncovered here in NGC 5548 may be related to intermittent periodic phenomena seen in the subclass of AGNs that have double-peaked Balmer emission

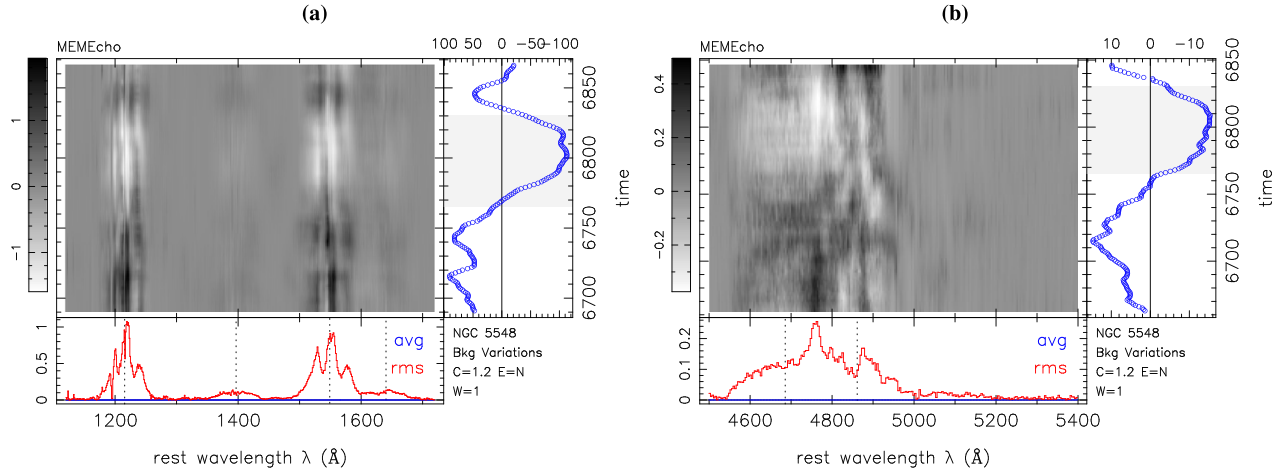

Figure 10. Slowly varying background component $L_0(\lambda, t)$ of the MEMECHO model fitted to the HST data (left) and MDM data (right). The model's time-averaged spectrum has been subtracted to leave time-varying residuals. The right panels show the wavelength-averaged response, with gray shading indicating the BLR Holiday dates. The bottom panels show the mean (blue) and rms (red) of the time-dependent residuals at each wavelength. All lines show a depressed flux during the BLR Holiday. The helical Barber-Pole pattern, with stripes moving from red to blue across the line profile, is evident in the C IV and Lyα residuals. The Barber-Pole pattern is absent in He II and may be present in Hβ but with a less clear pattern.

lines. In these double-peaked emitters there is a clear separation between the narrow emission lines and the broad double-peaked lines. The double-peaked velocity profiles can be modeled by emission from a Keplerian disk, with relativistic effects making the blue peak stronger and sharper than the red one and redshifting the line center. Spectroscopic monitoring of Arp 102B during 1987–1996 detected Hβ profile variations (Newman et al. 1997). In particular, during 1991–1995, the Hβ red/blue flux ratio oscillates over nearly 2 cycles of a 2.2 yr period, suggesting a patch of enhanced emission on a circular orbit within the disk. Contemporaneous monitoring of Hα during 1992–1996 shows that its red/blue flux ratio also oscillates by $\pm$10% with a 2 yr period (Sergeev et al. 2000). A trailed spectrogram display of the Hα residuals, after subtracting scaled mean line profiles, reveals a helical Barber-Pole pattern with two stripes that move from red to blue across the double-peaked Hα profile. This is strikingly similar to what we see in the C IV profile of NGC 5548. Similar phenomena are seen in other double-peaked emitters (Gezari et al. 2007; Lewis et al. 2010; Schimoia et al. 2015, 2017). Our discovery of the Barber-Pole pattern in NGC 5548 indicates that this phenomenon is not limited to the double-peaked emitters.

6. Summary

In this paper, we achieve the primary goal of the AGN STORM campaign by recovering velocity–delay maps for the prominent, broad, Lyα, C IV, He II, and Hβ emission lines in NGC 5548. These are the most detailed velocity–delay maps yet obtained for an AGN, providing unprecedented information on the geometry, ionization structure, and kinematics of the broad-line region.

Our analysis interprets the ultraviolet HST spectra (Paper I) and optical MDM spectra (Paper V) secured in 2014 during the 6-month STORM campaign on NGC 5548. This data set provides spectrophotometric monitoring of NGC 5548 with unprecedented duration, cadence, and S/N suitable for interpretation in terms of reverberations in the BLRs surrounding the black hole. Assuming that the time delays arise from light-travel time, the velocity–delay maps we construct from the reverberating spectra provide two-dimensional projected images of the BLR, one for each line, resolved on isodelay paraboloids and line-of-sight velocity.

We used the absorption-line modeling results from Paper VIII to divide out absorption lines affecting the HST spectra. We used PREPSPEC to recalibrate the flux, wavelength, and spectral resolution of the optical MDM spectra using the strong narrow emission lines as internal calibrators. Residuals from the PREPSPEC fits indicate the success of the calibration adjustments.

The linearized echo model that we normally use for echo mapping is violated in the STORM data set by anomalous emission-line behavior, the BLR Holiday discussed in Paper IV. We model this adequately as a slowly varying background spectrum superimposed on which are the more rapid variations due to reverberations.

The residuals of the PREPSPEC fits reveal significant emission-line profile changes. Features are evident moving inward from both red and blue wings toward the center of the Hβ line, interpretable as reverberations of a BLR with a Keplerian velocity field.

A helical "Barber-Pole" pattern with stripes moving from red to blue across line profile is evident in the C IV and possibly also the Lyα lines, suggesting an azimuthal structure rotating with a period of $\sim$2 yr around the far side of the accretion disk. This may be due to precession or orbital motion of disk structures. Similar behavior is seen in the double-peaked emitters, such as Arp 102B. Further HST observations of NGC 5548 over a multiyear time span, with a cadence of perhaps 10 days rather than 1 day, could be an efficient way to explore the persistence, transience, and nature of this new phenomenon in NGC 5548.

We use the PREPSPEC fit to extract light curves for the lines and continua and use MEMECHO to fit these light curves using the 1150 Å continuum light curve as a proxy for the driving light curve. The MEMECHO fit determines a set of echo maps $\Psi(\tau)$ giving the delay distribution of each echo, effectively slicing up the reverberating region on isodelay paraboloids. The structure in these echo maps indicates radial stratification, with He II responding from inside 5 lt-day and the Lyα C IV, and Hβ response extending out to or beyond 20 lt-day.

By using MEMECHO to fit reverberations in the emission-line profiles, we construct velocity–delay maps $\Psi(v, \tau)$ that

resolve the BLR in time delay and line-of-sight velocity. The BLR response is confined within a virial envelope around each line, with double-peaked velocity profiles in the response in delay slices of 10–20 days. The "M"-shaped changes in delay with velocity, found using velocity-resolved cross-correlation lags in Papers I and V, are seen here to be the signature of a Keplerian disk. The outer legs of the "M" arise from the virial envelope between 5 and 20 days; the inner "U" of the "M" is the lower part of an ellipse extending from 5 to 35 days. This velocity–delay structure is most straightforwardly interpreted as arising from a Keplerian disk extending from $R/c = 5$ to 20 days, inclined by $i \approx 45°$, and centered on a black hole of mass $M_{\rm BH} \approx 7 \times 10^7\, M_\odot$. The BLR has a well-defined outer rim at $R/c \approx 20$ days, but the far side of the rim may be obscured or less responsive than the near side.

Detailed modeling of the STORM data, guided by the features in the velocity–delay maps presented here, should be able to refine and quantify uncertainties on these features of the BLR, the inclination, and the black hole mass.

Support for HST program No. GO-13330 was provided by NASA through a grant from the Space Telescope Science Institute, which is operated by the Association of Universities for Research in Astronomy, Inc., under NASA contract NAS5-26555. K.H. acknowledges support from STFC grant ST/R000824/1. G.D.R., B.M.P., M.M.F, C.J.G., and R.W.P. are grateful for the support of the National Science Foundation (NSF) through grant AST-1008882 to The Ohio State University. Research at UC Irvine has been supported by NSF grants AST-1412693 and AST-1907290. M.C. Bentz gratefully acknowledges support through NSF CAREER grant AST-1253702 to Georgia State University. V.N.B. gratefully acknowledges assistance from National Science Foundation (NSF) Research at Undergraduate Institutions (RUI) grant AST-1909297. S.B. is supported by NASA through Chandra award AR7-18013X issued by the Chandra X-ray Observatory Center, operated by the Smithsonian Astrophysical Observatory for and on behalf of NASA under contract NAS8-03060. S.B. was also partially supported by grant HST-AR-13240.009. M.C. Bottorff acknowledges HHMI for support through an undergraduate science education grant to Southwestern University. E.M.C., E.D.B., L.M., and A.P. acknowledge support from Padua University through grants DOR1699945/16, DOR1715817/17, DOR1885254/18, and BIRD164402/16. G.F. and M. Dehghanian acknowledge support from the NSF (AST-1816537), NASA (ATP 17-0141), and STScI (HST-AR-13914, HST-AR-15018), and the Huffaker Scholarship. K.D.D. is supported by an NSF Fellowship awarded under grant AST-1302093. R.E. gratefully acknowledges support from NASA under ADAP award 80NSSC17K0126. P.A.E. acknowledges UKSA support. Support for A.V.F.'s group at UC Berkeley is provided by NSF grant AST-1211916, the TABASGO Foundation, the Christopher R. Redlich Fund, and the Miller Institute for Basic Research in Science. J.M.G. gratefully acknowledges support from NASA under awards NNX15AH49G and 80NSSC17K0126. P.B.H. is supported by NSERC. M.I. acknowledges support from the National Research Foundation of Korea (NRF) grant, No. 2020R1A2C3011091. M.D.J. acknowledges NSF grant AST-0618209. M.K. was supported by the National Research Foundation of Korea (NRF) grant funded by the Korea government (MSIT) (No. 2017R1C1B2002879). SRON is financially supported by NWO, the Netherlands Organization for Scientific Research. C.S.K. is supported by NSF grants AST-1515876 and AST-1814440. Y.K. acknowledges support from DGAPA-PAIIPIT grant IN106518. D.C.L. acknowledges support from NSF grants AST-1009571 and AST-1210311. P.L. acknowledges support from Fondecyt grant 1120328. A.P. is supported by NASA through Einstein Postdoctoral Fellowship grant No. PF5-160141 awarded by the Chandra X-ray Center, which is operated by the Smithsonian Astrophysical Observatory for NASA under contract NAS8-03060. J.S.S. acknowledges CNPq, National Council for Scientific and Technological Development (Brazil) for partial support and The Ohio State University for warm hospitality. T.T. has been supported by NSF grant AST-1412315. T.T. and B.C.K. acknowledge support from the Packard Foundation in the form of a Packard Research Fellowship to T.T. The American Academy in Rome and the Observatory of Monteporzio Catone are thanked by T.T. for kind hospitality. M.V. gratefully acknowledges support from the Independent Research Fund Denmark via grant Nos. DFF 4002-00275 and 8021-00130. J.-H.W. acknowledges support by the National Research Foundation of Korea (NRF) grant funded by the Korean government (No. 2010-0027910). This research has made use of the NASA/IPAC Extragalactic Database (NED), which is operated by the Jet Propulsion Laboratory, California Institute of Technology, under contract with the National Aeronautics and Space Administration. Research at Lick Observatory is partially supported by a generous gift from Google.

ORCID iDs

Keith Horne https://orcid.org/0000-0003-1728-0304
G. De Rosa https://orcid.org/0000-0003-3242-7052
B. M. Peterson https://orcid.org/0000-0001-6481-5397
A. J. Barth https://orcid.org/0000-0002-3026-0562
J. Ely https://orcid.org/0000-0002-4814-5511
M. M. Fausnaugh https://orcid.org/0000-0002-9113-7162
G. A. Kriss https://orcid.org/0000-0002-2180-8266
M. C. Bentz https://orcid.org/0000-0002-2816-5398
E. M. Cackett https://orcid.org/0000-0002-8294-9281
R. Edelson https://orcid.org/0000-0001-8598-1482
M. Eracleous https://orcid.org/0000-0002-3719-940X
M. R. Goad https://orcid.org/0000-0002-2908-7360
C. J. Grier https://orcid.org/0000-0001-9920-6057
C. S. Kochanek https://orcid.org/0000-0001-6017-2961
Y. Krongold https://orcid.org/0000-0001-6291-5239
S. Mathur https://orcid.org/0000-0002-4822-3559
H. Netzer https://orcid.org/0000-0002-6766-0260
D. Proga https://orcid.org/0000-0002-6336-5125
N. Tejos https://orcid.org/0000-0002-1883-4252
M. Vestergaard https://orcid.org/0000-0001-9191-9837
C. Villforth https://orcid.org/0000-0002-8956-6654
S. M. Adams https://orcid.org/0000-0001-5855-5939
P. Arévalo https://orcid.org/0000-0001-8503-9809
T G. Beatty https://orcid.org/0000-0002-9539-4203
V. N. Bennert https://orcid.org/0000-0003-2064-0518
S. Bisogni https://orcid.org/0000-0003-3746-4565
T. A. Boroson https://orcid.org/0000-0001-9481-1805
W. N. Brandt https://orcid.org/0000-0002-0167-2453
A. A. Breeveld https://orcid.org/0000-0002-0001-7270
M. Brotherton https://orcid.org/0000-0002-1207-0909
G. Canalizo https://orcid.org/0000-0003-4693-6157
M. T. Carini https://orcid.org/0000-0001-8961-2465
E. M. Corsini https://orcid.org/0000-0003-3460-5633
D. M. Crenshaw https://orcid.org/0000-0002-6465-3639
S. Croft https://orcid.org/0000-0003-4823-129X

K. V. Croxall https://orcid.org/0000-0002-5258-7224
E. Dalla Bontà https://orcid.org/0000-0001-9931-8681
A. J. Deason https://orcid.org/0000-0001-6146-2645
M. Dehghanian https://orcid.org/0000-0002-0964-7500
A. De Lorenzo-Cáceres https://orcid.org/0000-0002-9744-3486
C. Done https://orcid.org/0000-0002-1065-7239
P. A. Evans https://orcid.org/0000-0002-8465-3353
G. J. Ferland https://orcid.org/0000-0003-4503-6333
A. V. Filippenko https://orcid.org/0000-0003-3460-0103
O. D. Fox https://orcid.org/0000-0003-2238-1572
E. L. Gates https://orcid.org/0000-0002-3739-0423
J. M. Gelbord https://orcid.org/0000-0001-9092-8619
V. Gorjian https://orcid.org/0000-0002-8990-2101
J. E. Greene https://orcid.org/0000-0002-5612-3427
D. Grupe https://orcid.org/0000-0002-9961-3661
P. B. Hall https://orcid.org/0000-0002-1763-5825
C. B. Henderson https://orcid.org/0000-0001-8877-9060
E. Holmbeck https://orcid.org/0000-0002-5463-6800
T. W.-S. Holoien https://orcid.org/0000-0001-9206-3460
T. Hutchison https://orcid.org/0000-0001-6251-4988
M. Im https://orcid.org/0000-0002-8537-6714
M. D. Joner https://orcid.org/0000-0003-0634-8449
S. Kaspi https://orcid.org/0000-0002-9925-534X
P. L. Kelly https://orcid.org/0000-0003-3142-997X
J. A. Kennea https://orcid.org/0000-0002-6745-4790
S. Kim https://orcid.org/0000-0001-7052-6647
S. C. Kim https://orcid.org/0000-0001-9670-1546
A. King https://orcid.org/0000-0001-5352-0550
K. T. Korista https://orcid.org/0000-0003-0944-1008
M. W. Lau https://orcid.org/0000-0001-9755-9406
P. Lira https://orcid.org/0000-0003-1523-9164
C. Lochhaas https://orcid.org/0000-0003-1785-8022
Zhiyuan Ma https://orcid.org/0000-0003-3270-6844
M. A. Malkan https://orcid.org/0000-0001-6919-1237
J. C. Mauerhan https://orcid.org/0000-0002-7555-8741
R. McGurk https://orcid.org/0000-0003-2064-4105
L. Morelli https://orcid.org/0000-0001-6890-3503
J. A. Nousek https://orcid.org/0000-0001-7084-4637
A. Pancoast https://orcid.org/0000-0003-1065-5046
M. T. Penny https://orcid.org/0000-0001-7506-5640
A. Pizzella https://orcid.org/0000-0001-9585-417X
R. W. Pogge https://orcid.org/0000-0003-1435-3053
R. Poleski https://orcid.org/0000-0002-9245-6368
J.-U. Pott https://orcid.org/0000-0003-4291-2078
H.-W. Rix https://orcid.org/0000-0003-4996-9069
J. Runnoe https://orcid.org/0000-0001-8557-2822
D. A. Saylor https://orcid.org/0000-0002-0558-1305
J. S. Schimoia https://orcid.org/0000-0002-5640-6697
B. J. Shappee https://orcid.org/0000-0003-4631-1149
G. V. Simonian https://orcid.org/0000-0002-4230-6732
A. Skielboe https://orcid.org/0000-0001-9765-3603
G. Somers https://orcid.org/0000-0002-9322-0314
D. J. Stevens https://orcid.org/0000-0002-5951-8328
J. Tayar https://orcid.org/0000-0002-4818-7885
T. Treu https://orcid.org/0000-0002-8460-0390
C. S. Turner https://orcid.org/0000-0003-4400-5615
P. Uttley https://orcid.org/0000-0001-9355-961X
J. Van Saders https://orcid.org/0000-0002-4284-8638
J.-H. Woo https://orcid.org/0000-0002-8055-5465
H. Yan https://orcid.org/0000-0001-7592-7714
Y. Zu https://orcid.org/0000-0001-6966-6925

References

Bentz, M. C., Walsh, J. L., Barth, A. J., et al. 2009, ApJ, 705, 199
Blandford, R. D., & McKee, C. F. 1982, ApJ, 255, 419
Cackett, E. M., Horne, K., & Winkler, H. 2007, MNRAS, 380, 669
Chelouche, D., Pozo Nunez, F., & Kaspi, S. 2019, NatAs, 3, 251
Collier, S. J., Crenshaw, D. M., Peterson, B. M., et al. 2001, ApJ, 561, 146
De Rosa, G., Peterson, B. M., Ely, J., et al. 2015, ApJ, 806, 128
Dehghanian, M., Ferland, G. J., Kriss, G. A., et al. 2019a, ApJ, 877, 119
Dehghanian, M., Ferland, G. J., Peterson, B. M., et al. 2019b, ApJL, 882, L30
Edelson, R., Gelbord, J. M., Horne, K., et al. 2015, ApJ, 810, 129
Eracleous, M., & Halpern, J. P. 1994, ApJS, 90, 1
Eracleous, M., & Halpern, J. P. 2003, ApJ, 599, 886
Fausnaugh, M. M., Denney, K. D., Barth, A. J., et al. 2016, ApJ, 821, 56
Gardner, E., & Done, C. 2017, MNRAS, 470, 2245
Gezari, S., Halpern, J. P., & Eracleous, M. 2007, ApJS, 169, 167
Goad, M. R., Korista, K. T., De Rosa, G., et al. 2016, ApJ, 824, 11
Grier, C. J., Peterson, B. M., Horne, K., et al. 2013, ApJ, 764, 47
Horne, K. 1994, in ASP Conf. Ser. 69, Reverberation Mapping of the Broad-Line Region in Active Galactic Nuclei, ed. P. M. Gondhalekar, K. Horne, & B. M. Peterson (San Francisco, CA: ASP), 23
Horne, K., Peterson, B. M., Collier, S. J., & Netzer, H. 2004, PASP, 116, 465
Jarvis, M. J., & McLure, R. J. 2006, MNRAS, 369, 182
Korista, K. T., & Goad, M. R. 2019, MNRAS, 489, 5284
Kriss, G. A., De Rosa, G., Ely, J., Peterson, B. M., et al. 2019, ApJ, 881, 153
Lawther, D., Goad, M. R., Korista, K. T., Ulrich, O., & Vestergaard, M. 2018, MNRAS, 481, 533
Lewis, K. T., Eracleous, M., & Storchi-Bergmann, T. 2010, ApJS, 187, 416
Mangham, S. W., Knigge, C., Williams, P., et al. 2019, MNRAS, 488, 2780
Manser, C. M., Gänsicke, B. T., Eggl, S., et al. 2019, Sci, 364, 66
Marconi, A., Axon, D. J., Maiolino, R., et al. 2008, ApJ, 678, 693
Mathur, S., Gupta, A., Page, K., et al. 2017, ApJ, 846, 55
Morgan, C. W., Kochanek, C. S., Morgan, N. D., & Falco, E. E. 2010, ApJ, 712, 1129
Mosquera, A. M., Kochanek, C. S., Chen, B., et al. 2013, ApJ, 769, 53
Mummery, A., & Balbus, S. A. 2020, MNRAS, 492, 5655
Netzer, H., & Marziani, P. 2010, ApJ, 724, 318
Newman, J. A., Eracleous, M., Filippenko, A. V., & Halpern, J. P. 1997, ApJ, 485, 570
Pancoast, A., Brewer, B. J., Treu, T., et al. 2014, MNRAS, 445, 3073
Pei, L., Fausnaugh, M. M., Barth, A. J., et al. 2017, ApJ, 837, 131
Peterson, B. M. 1993, PASP, 105, 247
Peterson, B. M. 2014, SSRv, 183, 253
Peterson, B. M., Denney, K. D., De Rosa, G., et al. 2013, ApJ, 779, 109
Peterson, B. M., Ferrarese, L., Gilbert, K. M., et al. 2004, ApJ, 613, 682
Poindexter, S., Morgan, N., & Kochanek, C. S. 2008, ApJ, 673, 34
Schimoia, J. S., Storchi-Bergmann, T., Grupe, D., et al. 2015, ApJ, 800, 63
Schimoia, J. S., Storchi-Bergmann, T., Winge, C., Nemmen, R. S., & Eracleous, M. 2017, MNRAS, 472, 2170
Sergeev, S. G., Pronik, V. I., & Sergeeva, E. A. 2000, A&A, 356, 41
Shakura, N. I., & Sunyaev, R. A. 1973, A&A, 24, 337
Smith, J. D., Robinson, A., Alexander, D. M., et al. 2004, MNRAS, 350, 140
Starkey, D., Horne, K., Fausnaugh, M. M., et al. 2016, ApJ, 835, 65
Storchi-Bergmann, T., Schimoia, J. S., Peterson, B. M., et al. 2017, ApJ, 835, 236
Strateva, I. V., Strauss, M. A., Hao, L., et al. 2003, AJ, 126, 1720
Sturm, E., Dexter, J., Pfuhl, O., et al. 2018, Natur, 563, 657
Sun, M., Xue, Y., Guo, H., et al. 2020, ApJ, 891, 178
Vestergaard, M., Wilkes, B. J., & Barthel, P. D. 2000, ApJ, 538, L103
Walsh, J. L., Minezaki, T., Benz, M. C., et al. 2009, ApJS, 185, 156
Welsh, W. F., & Horne, K. 1991, ApJ, 379, 586
Wills, B. J., & Browne, I. W. A. 1986, ApJ, 302, 56
Xiao, M., Du, P., Lu, K. -K., et al. 2018, ApJL, 865, L8
Young, S., Axon, D. J., Robinson, A., Hough, J. H., & Smith, J. E. 2007, Natur, 450, 74